

# Wind- and Wave-Driven Reynolds Stress and Velocity Shear in the Upper Ocean for Idealized Misaligned Wind-Wave Conditions

DONG WANG<sup>a,b</sup> AND TOBIAS KUKULKA<sup>a</sup>

<sup>a</sup> *University of Delaware, Newark, Delaware*

(Manuscript received 16 July 2020, in final form 30 November 2020)

**ABSTRACT:** This study investigates the dynamics of velocity shear and Reynolds stress in the ocean surface boundary layer for idealized misaligned wind and wave fields using a large-eddy simulation (LES) model based on the Craik–Leibovich equations, which captures Langmuir turbulence (LT). To focus on the role of LT, the LES experiments omit the Coriolis force, which obscures a stress–current–relation analysis. Furthermore, a vertically uniform body force is imposed so that the volume-averaged Eulerian flow does not accelerate but is steady. All simulations are first spun-up without wind-wave misalignment to reach a fully developed stationary turbulent state. Then, a crosswind Stokes drift profile is abruptly imposed, which drives crosswind stresses and associated crosswind currents without generating volume-averaged crosswind currents. The flow evolves to a new stationary state, in which the crosswind Reynolds stress vanishes while the crosswind Eulerian shear and Stokes drift shear are still present, yielding a misalignment between Reynolds stress and Lagrangian shear (sum of Eulerian current and Stokes drift). A Reynolds stress budgets analysis reveals a balance between stress production and velocity–pressure gradient terms (VPG) that encloses crosswind Eulerian shear, demonstrating a complex relation between shear and stress. In addition, the misalignment between Reynolds stress and Eulerian shear generates a horizontal turbulent momentum flux (due to correlations of along-wind and crosswind turbulent velocities) that can be important in producing Reynolds stress (due to correlations of horizontal and vertical turbulent velocities). Thus, details of the Reynolds stress production by Eulerian and Stokes drift shear may be critical for driving upper-ocean currents and for accurate turbulence parameterizations in misaligned wind-wave conditions.

**KEYWORDS:** Langmuir circulation; Turbulence; Waves, oceanic; Large eddy simulations

## 1. Introduction

Langmuir turbulence (LT) is an important turbulent process in the ocean surface boundary layer (OSBL), which is driven by the Craik–Leibovich (CL) vortex force due to the wave–current interaction (Craik and Leibovich 1976). The structure of LT features coherent vortex pairs, which generates strong surface convergent regions and downwelling jets that significantly enhance vertical mixing (Thorpe 2004; Weller and Price 1988; Farmer and Li 1995). Previous studies have used large-eddy simulation (LES) models based on the filtered CL equation to investigate LT effects. These studies find that LT significantly increases the mixed layer deepening and induces stronger vertical velocity variance, which agrees well with observations (Gargett et al. 2004; Kukulka et al. 2009, 2010; D’Asaro 2014; Rabe et al. 2015). Furthermore, LT-enhanced mixing homogenizes the near-surface current shear, reducing the magnitude of the surface currents that play an important role in surface energy input (McWilliams et al. 1997; Wang et al. 2018). The stronger mixing also affects the flow structure in the Ekman layer, resulting in a slower decay of Ekman spiral with depth (McWilliams and Sullivan 2000; Polton et al. 2013).

Given the important role of LT in the OSBL, LT effects need to be parameterized and implemented into ocean models

that are based on Reynolds-averaged Navier–Stokes equations (RANS). For instance, the LT-enhanced mixing is parameterized by an enhancement factor applied to the turbulent eddy viscosity in the  $K$ -profile parameterization (KPP) model (McWilliams and Sullivan 2000; Reichl et al. 2016). Reynolds stress parameterizations based on the Lagrangian shear, rather than the Eulerian shear, have been proposed previously (McWilliams and Sullivan 2000; McWilliams et al. 2012). Such parameterizations have been tested in limited conditions, where the Reynolds stress is found to be well aligned with the Lagrangian shear (Reichl et al. 2016; Wang et al. 2019). However, a Reynolds stress parameterization based on shear and a single eddy viscosity coefficient usually disguises the dependency of stress on turbulence, currents, and wave forcing. For example, nonlocal transport plays a role in the misalignment between stress and Lagrangian shear for misaligned wind and wave conditions (Wang et al. 2019; Large et al. 2019). Another important reason for the stress–shear misalignment is that Reynolds stresses are produced at different rates due to Eulerian and Stokes drift shear (Harcourt 2013). The latter is the focus of this study.

Harcourt (2013, 2015) included the CL vortex force in Reynolds stress transport equations with the goal of developing a second moment turbulence closure scheme. These transport equations highlight that the Reynolds stress is not only produced by Eulerian shear, but also by Stokes drift shear and, at least partially, balanced by pressure terms. Thus, the Reynolds stress is not only related to Eulerian but also to Stokes drift shear, providing a theoretical motivation for the empirical relation between stress and Lagrangian shear. However, the work by

<sup>b</sup> Current affiliation: Bedford Institute of Oceanography, Dartmouth, Nova Scotia, Canada.

Corresponding author: Dong Wang, dongwang@udel.edu

Harcourt (2013, 2015) also indicates that the stress depends differently on Eulerian and Stokes drift shear, i.e., is not simply related to the sum of both shears (Lagrangian shear), which requires further investigations for more comprehensive stress parameterizations. This is also suggested by Pearson et al. (2019), which proposes a modified closure model for pressure terms.

One challenge in interpreting LES results of the OSBL is the presence of the Coriolis force, which not only causes rotation of currents and stresses, but also induces an Eulerian Stokes current due to the Coriolis–Stokes force (Polton et al. 2005). By omitting the Coriolis force, the LES experiments by Pearson (2018) overcome this challenge and clearly indicate that the presence of the Stokes drift induces an Eulerian countercurrent without the presence of the Coriolis–Stokes force. This countercurrent has no depth-integrated transport but is largely balanced by the Stokes drift near the surface (Teixeira 2018). While these experiments illustrate the relation between stress and currents, the statistical analysis of turbulence is more challenging because experiments are nonstationary without Coriolis force. Furthermore, none of these experiments or second-order closure schemes is conducted for strongly misaligned wind and waves, which is, however, a common situation in the real oceans (Fan et al. 2009).

Building on earlier work, this study designs idealized LES experiments that are stationary but do not include the Coriolis force, to facilitate a stress–shear analysis in the presence of LT (section 2). In the results section, we examine the evolution of stress and Lagrangian shear, which are under substantial wind-wave misalignments (section 3). The goal of this study is to improve our understanding of the stress–current shear relationship, which is not only fundamental to upper-ocean turbulence dynamics but also the corner stone for practical ocean models that are used for weather, climate, and pollution fate projections.

## 2. Methods

### a. LES model with a body force

We employ a large-eddy simulation model to simulate OSBL turbulence. The LES model solves the filtered CL equations (McWilliams et al. 1997)

$$\frac{\partial \mathbf{u}}{\partial t} + \mathbf{u} \cdot \nabla \mathbf{u} = \mathbf{F}_b - \frac{\rho}{\rho_0} \mathbf{g} - \nabla \pi + \mathbf{u}_s \times \boldsymbol{\omega} + \text{SGS}, \quad (1)$$

where  $\mathbf{u} = (u, v, w)$  is the resolved velocity vector with components in the  $x, y, z$  directions, which denote the along-wind, crosswind, and vertical coordinates ( $z$  is positive up and  $z = 0$  at the sea surface), respectively;  $\mathbf{F}_b$  is a body force discussed below;  $\rho$  is the water density, and  $\rho_0 = 1027 \text{ kg m}^{-3}$  is a reference density;  $\mathbf{g} = (0, 0, g)$  is the gravity acceleration vector, and  $g = 9.81 \text{ m s}^{-2}$ ;  $\pi = 1/2[(\mathbf{u} + \mathbf{u}_s) \cdot (\mathbf{u} + \mathbf{u}_s) - \mathbf{u} \cdot \mathbf{u}] + p/\rho_0$  is a generalized pressure, and  $p$  is the pressure;  $\boldsymbol{\omega} = \nabla \times \mathbf{u}$  is the vorticity; SGS represents subgrid-scale terms;  $\mathbf{u}_s = (u_s, v_s, 0)$  is the Stokes drift vector. We prescribe the profiles of  $\mathbf{u}_s$  based on a monochromatic wave

TABLE 1. Wave conditions for the LES experiments described in section 2b.

Case	STC	LT0	LT45	LT90
$u_s \text{ (m s}^{-1}\text{)}$	0	0.068	0.068	0
$v_s \text{ (m s}^{-1}\text{)}$	0	0	0.068	0.068

$$[u_s(z), v_s(z)] = [u_{s0} \exp(2kz), v_{s0} \exp(2kz)], \quad (2)$$

where  $(u_{s0}, v_{s0})$  is the surface Stokes drift vector in the along-wind and crosswind directions and  $k$  is wavenumber.

Since this study focuses on investigating the role of LT in determining the profiles of Reynolds stress and Eulerian currents, it is desirable to remove the Coriolis force that generates inertial oscillations, Ekman transport, and a complex Eulerian return flow through the Stokes–Coriolis interaction (Polton et al. 2005). This ensures that any generation of crosswind Eulerian currents can be only forced by internal crosswind stresses that redistribute crosswind momentum vertically without any net crosswind momentum forces. This facilitates the stress–shear analysis. However, without Coriolis force the wind stress is not balanced by other forces, so that the currents accelerate and LES solutions are nonstationary.

To remedy this, we add a constant body force  $\mathbf{F}_b$  over the OSBL depth  $H_B$  that opposes the wind stress. The horizontally averaged momentum equation becomes

$$\frac{\partial \langle \mathbf{u} \rangle}{\partial t} = \frac{1}{\rho_0} \frac{\partial \boldsymbol{\tau}}{\partial z} + \mathbf{F}_b, \quad (3)$$

where Reynolds stress vector is  $\boldsymbol{\tau} = (-\rho_0 \langle u'w' \rangle, -\rho_0 \langle v'w' \rangle, 0)$ , the symbol  $\langle \rangle$  denotes horizontal averages over the LES domain, and the prime indicates deviations from such averages. We set  $\mathbf{F}_b = (F_b, 0, 0) = (-H_B^{-1} u_*^2, 0, 0)$ , so that  $\mathbf{F}_b$  balances the surface wind stress. Here,  $u_*$  is the waterside friction velocity defined through  $|\boldsymbol{\tau}(z=0)| = \rho_0 u_*^2$ .

### b. Experiments with idealized wind-wave misalignments

We design four idealized LES experiments to assess the relation between Lagrangian shear and Reynolds stress. For all simulations, we impose a constant wind stress of  $0.037 \text{ N m}^{-2}$  ( $u_* = 6.1 \times 10^{-3} \text{ m s}^{-1}$ ) along the  $x$  direction, corresponding to a wind speed of about  $5 \text{ m s}^{-1}$ . The initial mixed layer depth is  $36 \text{ m}$ , which is above a stratified layer with a constant temperature gradient of  $0.04 \text{ K m}^{-1}$ . The body force is applied to all experiments as discussed above, so that the mixed layer depth is approximately constant. According to (3), the Reynolds stress decreases linearly from the surface to zero at the mixed layer base for stationary LES solutions. The computational domain is  $100 \text{ m}$  deep and  $150 \text{ m}$  wide in both  $x$  and  $y$  directions, with 256 vertical grid points and  $128 \times 128$  horizontal grids.

The four cases are characterized by different wave conditions (Table 1). We set the Stokes drift in case STC to zero as a control case that only captures shear-driven turbulence (ST). The cases with CL vortex force LT0, LT45, and LT90 include wind-wave misalignments of  $0^\circ$  [ $(u_{s0}, v_{s0}) = (0.068, 0) \text{ m s}^{-1}$ ],  $45^\circ$  [ $(u_{s0}, v_{s0}) = (0.068, 0.068) \text{ m s}^{-1}$ ], and  $90^\circ$  [ $(u_{s0}, v_{s0}) = (0, 0.068)$ ]

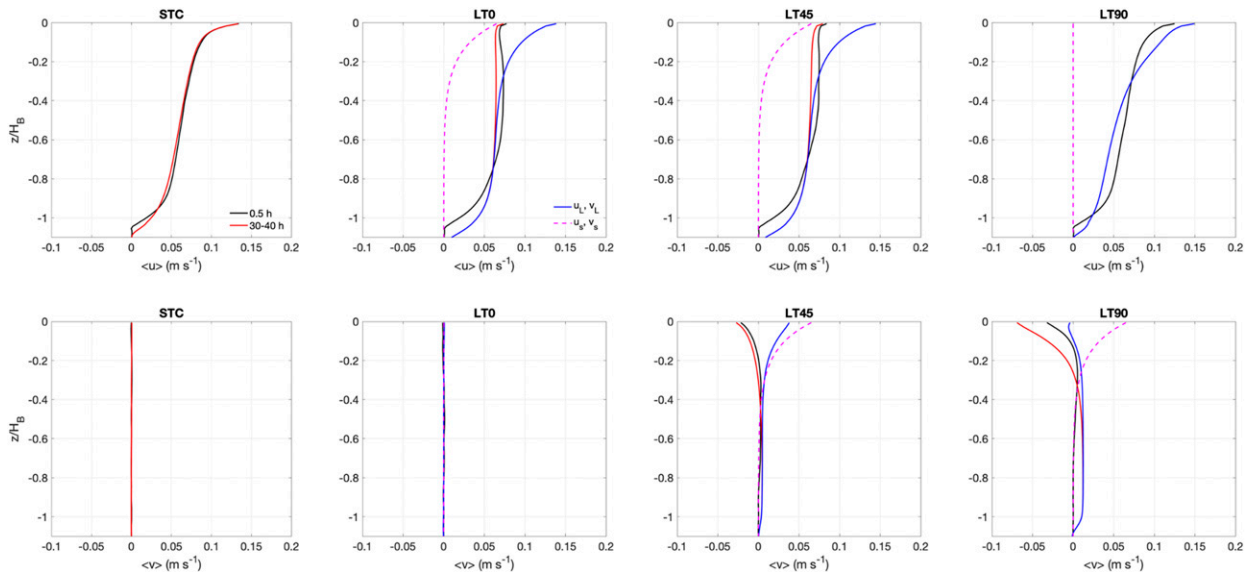


FIG. 1. Eulerian currents at  $t = 0.5$  h (black solid line), time-averaged Eulerian currents (red solid lines), and time-averaged Lagrangian currents (blue solid lines) in the (top) along-wind direction and (bottom) crosswind direction for cases STC, LT0, LT45, and LT90. The time average is done from  $t = 30$  h to  $t = 40$  h. The magenta dashed lines in cases LT0, LT45, and LT90 indicate the constant Stokes drift in the along-wind and crosswind directions. The depths hereinafter are all normalized by the mixed layer depth  $H_B$ .

$\text{m s}^{-1}$ ], respectively. The wavenumber is set to  $k = 0.105 \text{ m}^{-1}$ . The Stokes drift is chosen, so that the cases LT0 and LT45 have the same Stokes drift shear production, whereas case LT90 has zero Stokes drift shear production for the stationary solutions. For the aligned case LT0, the turbulent Langmuir number is  $\text{La}_\tau = \sqrt{u_{s0}/u_*} = 0.3$ , indicating a Langmuir turbulence regime (McWilliams et al. 1997).

Note that Pearson (2018) cautions about the applicability of the LES subgrid-scale scheme to strongly wind-wave misaligned cases. However, we find that our LES solutions are well resolved and only weakly dependent on the LES subgrid-scale closure scheme (Deardorff 1973; Moeng 1984; Sullivan et al. 1994), so that the conclusions presented here are robust in spite of potential shortcomings of the LES subgrid-scale closure scheme. The initial condition at  $t = 0$  for all four cases is given by a fully turbulent solution for forcing case STC without Stokes drift. For the cases with Stokes drift, the Stokes drift is abruptly imposed at  $t = 0$  so that LES solutions are first transient and develop to a new stationary state with CL forcing.

### 3. Results

We investigate the relation of Reynolds stress and Lagrangian shear through the LES experiments with idealized wind-wave misalignments, aiming to understand the influence of LT on the profiles of stress and mean currents. First, we briefly assess the profiles of Reynolds stress and mean currents. In the early transient stage of the simulations, Reynolds stress and Eulerian currents are generated in the crosswind direction for the wind-wave-misaligned cases. However, in the later stationary stage, the crosswind Reynolds stress vanishes but the crosswind Lagrangian shear is still present, yielding a

misalignment between Reynolds stress and Lagrangian shear (section 3a). We then focus on interpreting the stationary results guided by a budgets analysis for the Reynolds stress transport equation. Our results illustrate the important role of LT and the CL vortex force in generating Reynolds stress, which is not related to Lagrangian shear (section 3b) but can be generally parameterized by using two eddy viscosities that apply to the Eulerian shear and Stokes drift shear, respectively (section 3c). At the same time, we find the generation of a turbulent horizontal flux of horizontal momentum ( $\langle u'v' \rangle$ ) for the wind-wave misalignment cases, which is caused by the misalignment between Reynolds stress and Eulerian shear and reduces the stress production by Stokes drift shear in the direction of vertical turbulent momentum flux (section 3d).

#### a. Generation of crosswind Eulerian currents and Reynolds stresses

In this section, we briefly analyze the development of stress and current profiles, aiming to exhibit stress–shear misalignments for strongly misaligned wind and waves. Once the Stokes drift is imposed, profiles rapidly change within 2 h and reach a stationary state after 30 h for all cases (Figs. 1 and 2). Compared to case STC which is stationary, the along-wind Eulerian current in case LT0 is more uniform in the upper 25 m after 0.5 h due to the presence of LT, which enhances turbulent mixing and homogenizes the current shear (Fig. 1).

For case LT45, the along-wind current is similar to case LT0, suggesting similar mixing effects for both cases. However, an Eulerian current that opposes the Stokes drift is generated in the crosswind direction (LT45, bottom panel, Fig. 1). A crosswind Eulerian current is also found in case LT90 but crosswind currents differ, although both cases (LT45 and

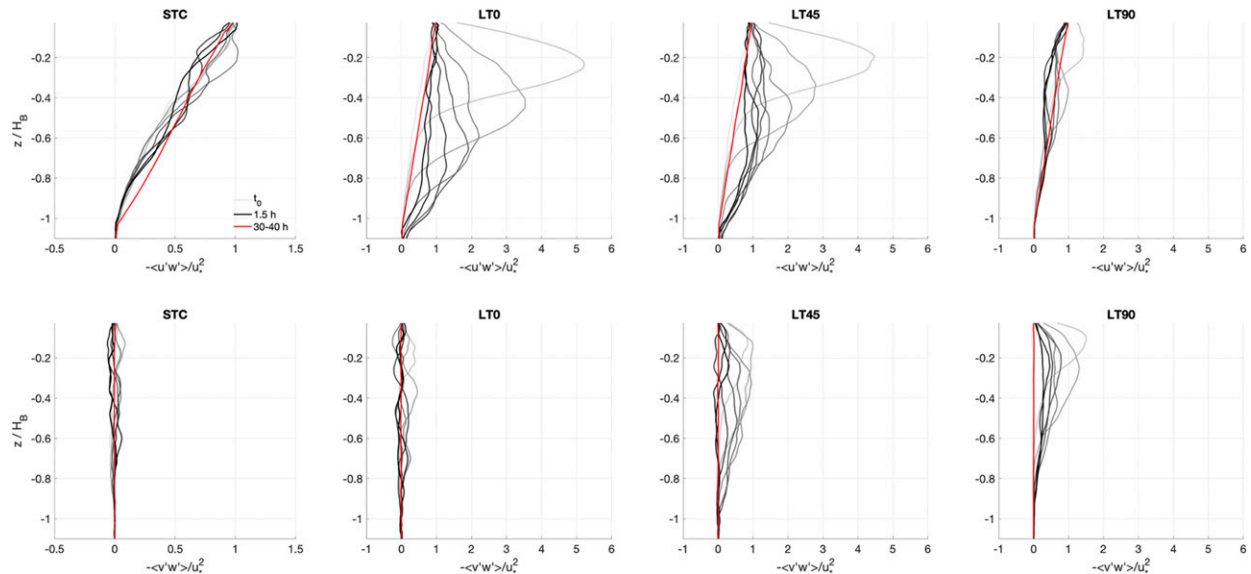


FIG. 2. (top) Along-wind and (bottom) crosswind turbulent momentum flux  $-\langle u_i'w' \rangle$  ( $i = 1, 2$ ) normalized by  $u_*^2$  (solid lines with color hue from light gray to black) from the first time point (light gray solid line) to  $t = 1.5$  h (black solid line), and each color represents a specific time point within the first 1.5 h. The red solid line indicates a time-averaged stress from  $t = 30$  h to  $t = 40$  h for cases STC, LT0, LT45, and LT90.

LT90) have the same crosswind Stokes drift. This is because turbulent mixing differs for the two cases. Thus, the counter-Stokes drift of crosswind Eulerian current is not solely dependent on the crosswind Stokes drift but can be also influenced by other factors that will be discussed in section 3b. In addition, we find that the depth-integrated  $\langle v \rangle$  over  $H_B$  is always zero (not shown here) for all cases, which is consistent with the expected momentum conservation in the absence of surface wind stress in the  $y$  direction. To examine if the crosswind Eulerian current vanishes over time, we also assess profiles of time-averaged Eulerian and Lagrangian currents when the flow is stationary (red solid and blue lines, Fig. 1). For both LT45 and LT90, the time-averaged crosswind Eulerian currents are nonnegligible and the magnitude of the crosswind Eulerian current in case LT90 even increases by twice at the surface compared to that at  $t = 0.5$  h (red solid lines, bottom panels, cases LT45 and LT90, Fig. 1). In addition, those crosswind Eulerian currents do not balance the Stokes drift, resulting in nonzero Lagrangian currents and associated shear in the crosswind direction for wind-misaligned wave cases (blue solid lines, bottom panels, cases LT45 and LT90, Fig. 1).

Since the only force that drives the crosswind Eulerian current is the interior crosswind Reynolds stress within the boundary layer, we examine the profiles of the Reynolds stress for all cases (Fig. 2). The Reynolds stress in case STC decays linearly in the along-wind direction and is approximately zero in the crosswind direction (STC, Fig. 2), as expected (see discussion above). For case LT0, right after imposing the wave forcing, the peak of the along-wind stress profile exceeds the surface value by a factor of about 5 (light gray solid line, LT0, Fig. 2). This is notably different

from typical stress profiles with the maximum stress at the surface and monotonically decreasing with depth. This peak decreases and deepens as the along-wind stress profile becomes close to its stationary profile at  $t = 1.5$  h (black and red solid lines, LT0, Fig. 2).

For case LT45, the along-wind Reynolds stress profile is close to LT0, which accounts for the similar profiles of along-wind Eulerian currents in both cases (LT0 and LT45, Fig. 2). Consistent with the crosswind velocity profiles, Reynolds stress is present in the crosswind direction for the wind-wave misalignment cases (LT45 and LT90), which drives the crosswind Eulerian currents. However, the crosswind Reynolds stress decays with time and is close to zero after 30 h for both case LT45 and LT90. Note that the profiles of stress and currents for all cases approach their stationary profiles after about 2 h. The adjustment time scale can be linked to an eddy turnover time scale, which is nontrivially related to  $u_*$  and the Stokes drift velocity profile (Harcourt and D'Asaro 2008; Wang et al. 2019; Kukulka and Veron 2019). This complex transient state is not the focus of this investigation but demonstrates the system's transition from the initial state without Stokes drift to a new stationary state subject of this study.

We next assess the time-averaged Reynolds stress profiles and investigate the potential misalignment between Reynolds stress and shear vectors, including the Lagrangian shear and Eulerian shear. For all four cases STC, LT0, LT45, and LT90, the stress in the along-wind direction linearly decreases with depth, and stress in the crosswind direction is about zero throughout the OSBL, which is expected in the wind-forced OSBL with stationary current shear (red solid lines, Fig. 2) (Wang et al. 2019). Note that the stress vector rotates and

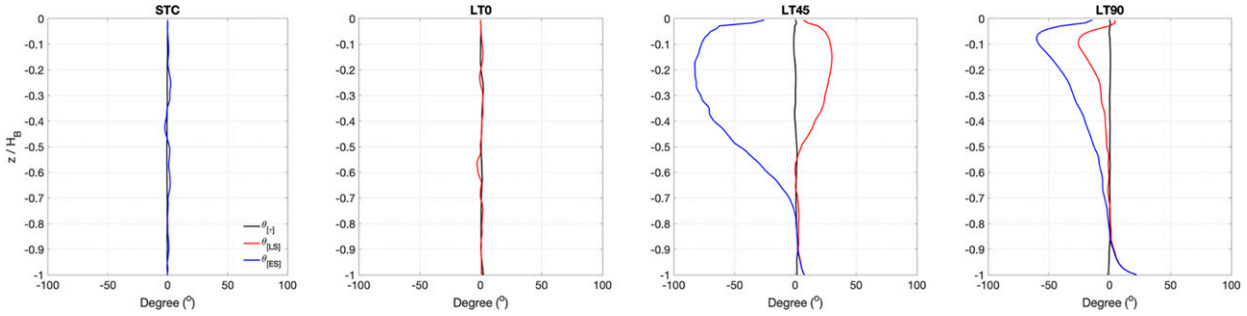


FIG. 3. The directions of Reynolds stress (black solid line), Eulerian shear (blue solid line), and Lagrangian shear (red solid line) averaged from  $t = 30$  h to  $t = 40$  h for experiments STC, LT0, LT45, and LT90.

decays with depth in the real oceans with the Coriolis force and thus is generally not aligned with the wind except at the surface.

For case STC, the stress is aligned with the Eulerian shear as expected in shear-driven turbulence (STC, Fig. 3). For case LT0, however, the Eulerian shear is near zero at  $-0.05H_B > z > -0.6H_B$  due to LT-enhanced upper-ocean mixing (red solid line, LT0, Fig. 1 and the direction of Eulerian shear is not shown in LT0, Fig. 3). As a result, the along-wind Stokes drift shear in LT0 dominates the Lagrangian shear at  $-0.05H_B > z > -0.6H_B$ , which is aligned with the Reynolds stress (LT0, Fig. 3). However, for case LT45, the misalignment between Lagrangian shear and Reynolds stress is more than  $30^\circ$ , although the wind-wave misalignment is only  $45^\circ$  (black and red solid lines, LT45, Fig. 3). Due to the presence of a negative  $\langle v \rangle$  and a vertically uniform along-wind Eulerian current (LT45, Fig. 1), the Eulerian shear in LT45 is along the negative  $y$  direction and about  $-90^\circ$  misaligned with the stress (blue solid line, LT45, Fig. 3). For case LT90, both the Lagrangian shear and Eulerian shear exhibit misalignments with the stress, even though case LT90 is characterized by weak LT as indicated by the mean currents discussed above (Fig. 1) and stress budgets discussed below (Fig. 5). Thus, our results demonstrate that Lagrangian shear is not necessarily aligned with the Reynolds stress in the presence of LT in wind-wave misalignment conditions, which is also found in the LES experiment forced by realistic wind and waves in the Southern Ocean (Large et al. 2019).

*b. Crosswind stress budgets under wind-wave misalignments*

To better understand the relation between the stress and shear vectors, in particular for the preserved crosswind Eulerian shears without crosswind stress, we examine the Reynolds stress transport equation for the cases with waves [refer to Eq. (5) in Harcourt (2013)]

$$\frac{\partial \langle u'w' \rangle}{\partial t} + \frac{\partial \langle u'w'w' \rangle}{\partial z} = -\langle w'w' \rangle \frac{\partial \langle u \rangle}{\partial z} - \left( \langle u'u' \rangle \frac{\partial u_s}{\partial z} + \langle u'v' \rangle \frac{\partial v_s}{\partial z} \right) - \frac{1}{\rho_0} \left( \left\langle u' \frac{\partial p'}{\partial z} \right\rangle + \left\langle w' \frac{\partial p'}{\partial x} \right\rangle \right) + \text{SGS}_x, \tag{4}$$

and

$$\frac{\partial \langle v'w' \rangle}{\partial t} + \frac{\partial \langle v'w'w' \rangle}{\partial z} = -\langle w'w' \rangle \frac{\partial \langle v \rangle}{\partial z} - \left( \langle v'v' \rangle \frac{\partial v_s}{\partial z} + \langle u'v' \rangle \frac{\partial u_s}{\partial z} \right) - \frac{1}{\rho_0} \left( \left\langle v' \frac{\partial p'}{\partial z} \right\rangle + \left\langle w' \frac{\partial p'}{\partial y} \right\rangle \right) + \text{SGS}_y, \tag{5}$$

where the left-hand side terms of Eqs. (4) and (5) represent, respectively, the temporal change rate of Reynolds stress (first term) and the vertical divergence of Reynolds stress flux due to vertical turbulent velocities (second term). The right-hand side (rhs) terms from left to right are stress production due to Eulerian shear (Pshear); stress production due to Stokes drift shear (Pstokes); velocity–pressure gradient terms (VPG) that redistribute energy of different fluctuation velocities in different directions, unresolved SGS terms in  $x$  ( $\text{SGS}_x$ ) and  $y$  ( $\text{SGS}_y$ ) directions. These stress budgets suggest that the Stokes drift induces an additional stress production, which accounts for the sudden increase of Reynolds stress in the along-wind direction [Eq. (4)] and the appearance of Reynolds stress in the crosswind direction [Eq. (5)]. To simplify the analysis, we only examine the budget terms that are time-averaged when the flow is stationary, which includes the stress production by Stokes drift shears (Pstokes), stress production by Eulerian shears (Pshear), the divergence of the Reynolds-stress flux and VPG (Fig. 5). Our goal is to reveal the shear–stress relation that is enclosed in the stress budgets.

Before we examine the stress budgets, we first assess profiles of velocity variances, which critically influence both Pshear and Pstokes (Fig. 4). In general, the profiles of velocity variances between cases LT0 and LT45 are close, which characterizes much greater crosswind velocity variances than the along-wind velocity variances and enhanced vertical velocity variances, suggesting a similar LT regime in both cases (black and red solid lines, Fig. 4). For LT90, however, the along-wind velocity variance is larger than the crosswind velocity variance and the vertical velocity variance is the smallest (blue solid line, Fig. 4), which is comparable to velocity variance profiles of shear-driven turbulence in case STC (blue dashed lines, Fig. 4). This is consistent with the examination of mean current profiles, which also indicates weak LT in LT90 (Fig. 1).

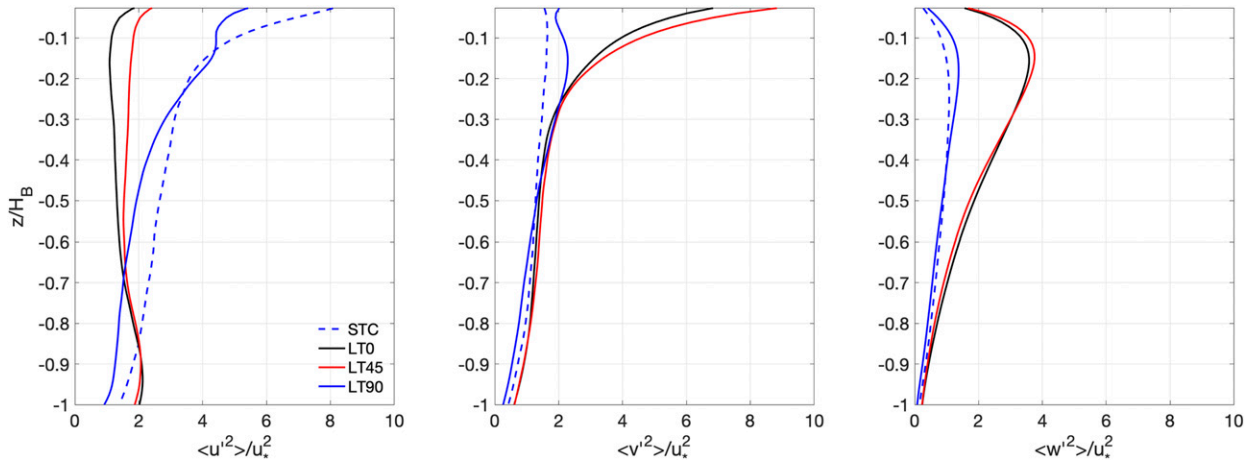


FIG. 4. Time-averaged and normalized (left) along-wind, (center) crosswind, and (right) vertical velocity variance profiles for case STC (blue dashed), LT0 (black solid), LT45 (red solid), and LT90 (blue solid). The velocity variances are normalized by  $u_*^2$  and time averaged from  $t = 30$  h to  $t = 40$  h.

For case LT0, the pronounced transport of Reynolds stress only occurs in the along-wind direction because of the absence of wind and wave forcing in the crosswind direction (left panels, Fig. 5). In the along-wind direction, the balance of stress budgets is mostly between  $P_{\text{Stokes}}$  and the VPG. Since

the LT-enhanced vertical mixing results in a near-zero Eulerian shear (case LT0, top panel, Fig. 1),  $P_{\text{shear}}$  is greatly reduced and much smaller than  $P_{\text{Stokes}}$ . One may expect that the along-wind stress budgets in case LT45 is similar to case LT0 given that both cases have the same along-wind Stokes

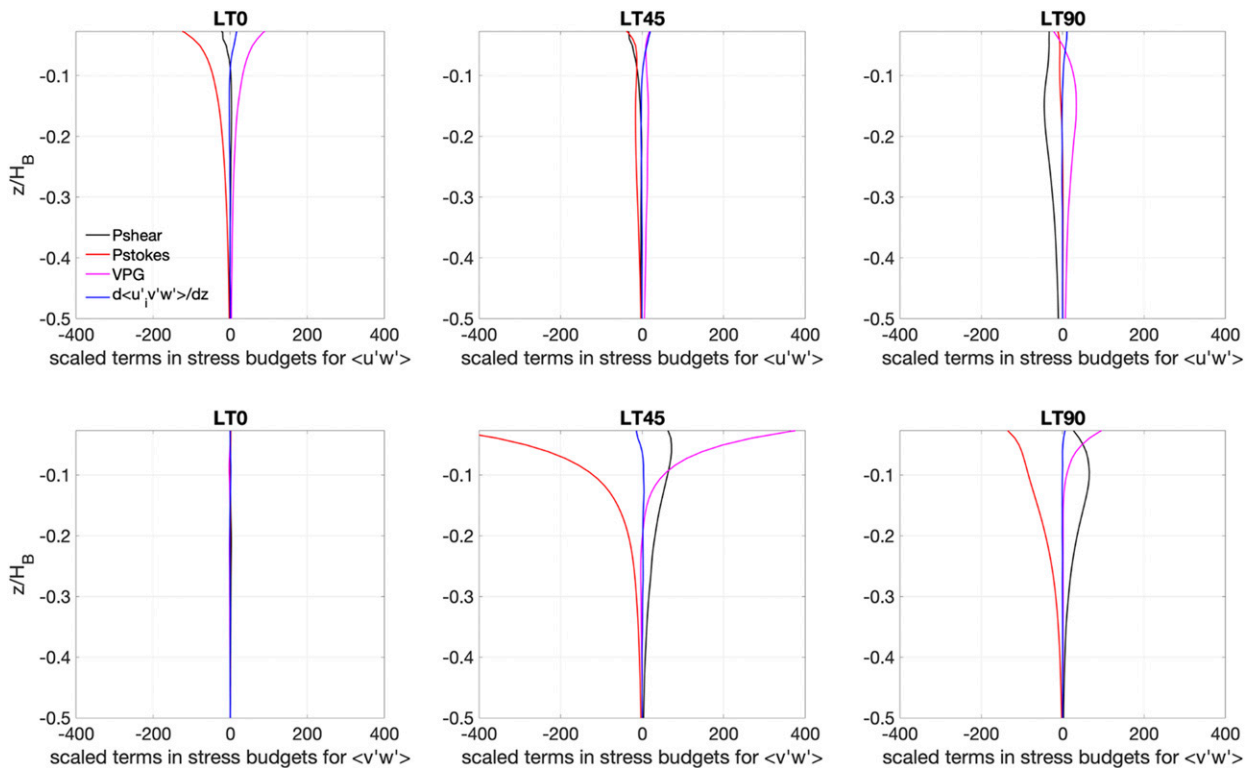


FIG. 5. Scaled terms in Reynolds stress budgets for (top)  $\langle u'w' \rangle$  and (bottom)  $\langle v'w' \rangle$  in cases (left) LT0, (center) LT45, and (right) LT90. All terms are scaled by  $u_*^3/H_B$  and are time averaged from  $t = 30$  h to  $t = 40$  h. The Eulerian shear stress production ( $P_{\text{shear}}$ ), Stokes drift shear stress production ( $P_{\text{Stokes}}$ ), VPG, and the vertical divergence of the Reynolds-stress flux ( $d\langle u'_i v'_i w' \rangle / dz$  and  $i = 1, 2$ ) are denoted by black, red, magenta, and blue solid lines.

drift and similar velocity variance profiles (black and red solid lines, Fig. 4). However,  $P_{\text{Stokes}}$  in case LT45 is found much smaller than case LT0 and is close to  $P_{\text{shear}}$  in the along-wind direction (left and center panels, Fig. 5). Recalling the  $P_{\text{Stokes}}$  term in Eq. (4), this suggests that in addition to profiles of velocity variances and Stokes drift,  $\langle u'v' \rangle$  is another important factor in controlling the stress production by waves, which will be further discussed in section 3c.

Different from LT0, terms in the crosswind stress budgets are nonnegligible for LT45 (bottom-center panel, Fig. 5), although the crosswind stress is close to zero (LT45, Fig. 2). Though the along-wind and crosswind Stokes drift are the same in case LT45 (red solid lines, center, Fig. 5), the crosswind  $P_{\text{Stokes}}$  is significantly greater than the along-wind  $P_{\text{Stokes}}$ , which is caused by the increased crosswind velocity variance from LT (red solid lines, left and center, Fig. 4). Furthermore, the stress production due to crosswind Eulerian shear is positive throughout the OSBL and its magnitude is greater than the along-wind stress production (center panels, Fig. 5), which is due to the presence of a negative gradient of crosswind Eulerian currents (case LT45, Fig. 1). Thus, this result indicates that current shear does not imply the presence of a net momentum flux. Specifically, this means that a nonzero Lagrangian current is present in the crosswind direction, which accounts for the misalignments between the Reynolds stress and Lagrangian shear in section 3a.

Likewise, the nonnegligible terms in the crosswind stress budgets are also observed for LT90. The positive stress production due to Eulerian shear also occurs in the crosswind direction in case LT90 but the magnitude of stress budgets in the crosswind direction in case LT90 are generally smaller than case LT45, particularly the crosswind Stokes drift shear production (bottom right, Fig. 5). Given that the crosswind Stokes drift is the same for cases LT45 and LT90, the difference in Stokes drift shear stress productions can be due to different  $\langle u'v' \rangle$  (section 3c) and different velocity variances (red and blue solid lines, middle panel, Fig. 4). In general, it is expected that the crosswind Eulerian currents are different between LT45 and LT90 because none of their stress budget terms in the crosswind direction is the same, in spite of the same crosswind Stokes drift. Thus, the emergence of the crosswind Eulerian current occurs due to changes in the turbulence (Fig. 4), which are reflected by the different stress budgets.

c. Comparison with Reynolds stress parameterizations

Since the presence of nonnegligible Lagrangian currents with near-zero stress also illustrates a noncausal relation between the Lagrangian shear and Reynolds stress, Reynolds stress parameterization with Lagrangian shear and a single eddy viscosity is not sufficient. To remedy this problem, recent studies introduce two different turbulent eddy viscosities:  $\nu_t$  and  $\nu_t^s$ , which apply to Eulerian shear and Stokes drift shear, respectively (Harcourt 2013, 2015; Pearson et al. 2019):

$$-\langle u'w' \rangle = \nu_t \frac{\partial \langle u \rangle}{\partial z} + \nu_t^s \frac{\partial u_s}{\partial z}, \tag{6}$$

and

$$-\langle v'w' \rangle = \nu_t \frac{\partial \langle v \rangle}{\partial z} + \nu_t^s \frac{\partial v_s}{\partial z}, \tag{7}$$

by which the new parameterization theoretically has the capability of capturing the misalignment between Lagrangian shear and Reynolds stress. The physics behind two different eddy viscosities are captured by the Reynolds stress transport equation (Harcourt 2013). The two eddy viscosities have been estimated with so-called algebraic Reynolds stress models (ARSMs) where the Reynolds stress is determined from the mean flow and turbulent kinetic energy (TKE). To include LT effects, Stokes drift shear stress production and the wave-averaged effects due to Stokes drift on VPG are also modeled in ARSMs (Harcourt 2013, 2015; Pearson et al. 2019).

To demonstrate the necessity of using two different eddy viscosities in the Reynolds stress parameterization, particularly wind-wave misalignment conditions, we use our LES results for the Reynolds stresses, Eulerian shears, and Stokes drift shears in Eqs. (6) and (7) in cases LT45 and LT90 to algebraically compute  $\nu_t^s$  and  $\nu_t$  (top panels, Fig. 6). For both cases LT45 and LT90,  $\nu_t^s$  and  $\nu_t$  are different throughout most depths except near the surface. In addition, the ratio of  $\nu_t^s$  to  $\nu_t$  differs for the two cases, illustrating its sea-state dependency (blue solid lines, bottom panels, Fig. 6). For comparison, we utilize the ARSM developed by Harcourt (2015) (hereinafter H15), where  $\nu_t^s/\nu_t$  equals  $S_M^s/S_M$ . The terms  $S_M^s$  and  $S_M$  are nondimensional stability functions [refer to Eqs. (33a) and (33c) in Harcourt 2015]. Note that the parameterization of H15 has not been developed specifically for substantial wind-wave misalignment conditions; nevertheless, this ARSM clearly highlights differences between  $\nu_t^s$  and  $\nu_t$  and their performance can be evaluated through the LES experiments from this study.

In general, H15 captures the vertical profile of  $\nu_t^s/\nu_t$  for both LT45 and LT90 cases, particularly the relative size between the two eddy viscosities in different sea states (bottom panels, Fig. 6). However, there still exist differences between the LES and H15 for both cases, especially near the surface, which is expected because of near-boundary and strong wind-wave misalignment effects. Harcourt's (2015) near-wall treatment model does not apply to wind-wave misalignment angles greater than  $\pi/6$ . For instance, the expression for the length scale in the surface-proximity function [Eq. (35) in Harcourt 2015] does not account for zero Stokes drift shear production as in the case LT90. The recent study by Pearson et al. (2019) further shows that the closure scheme for the pressure terms, which critically influences ARSM results, does not agree with LES results, even under wind-aligned wave conditions. Note that the eddy viscosity is parameterized through the product of a length scale, a velocity scale and a stability function, which is oversimplified according to the full Reynolds stress budgets (Harcourt 2013; Pearson et al. 2019). All these factors contribute to the difference of  $\nu_t^s/\nu_t$  between the LES results and H15, and

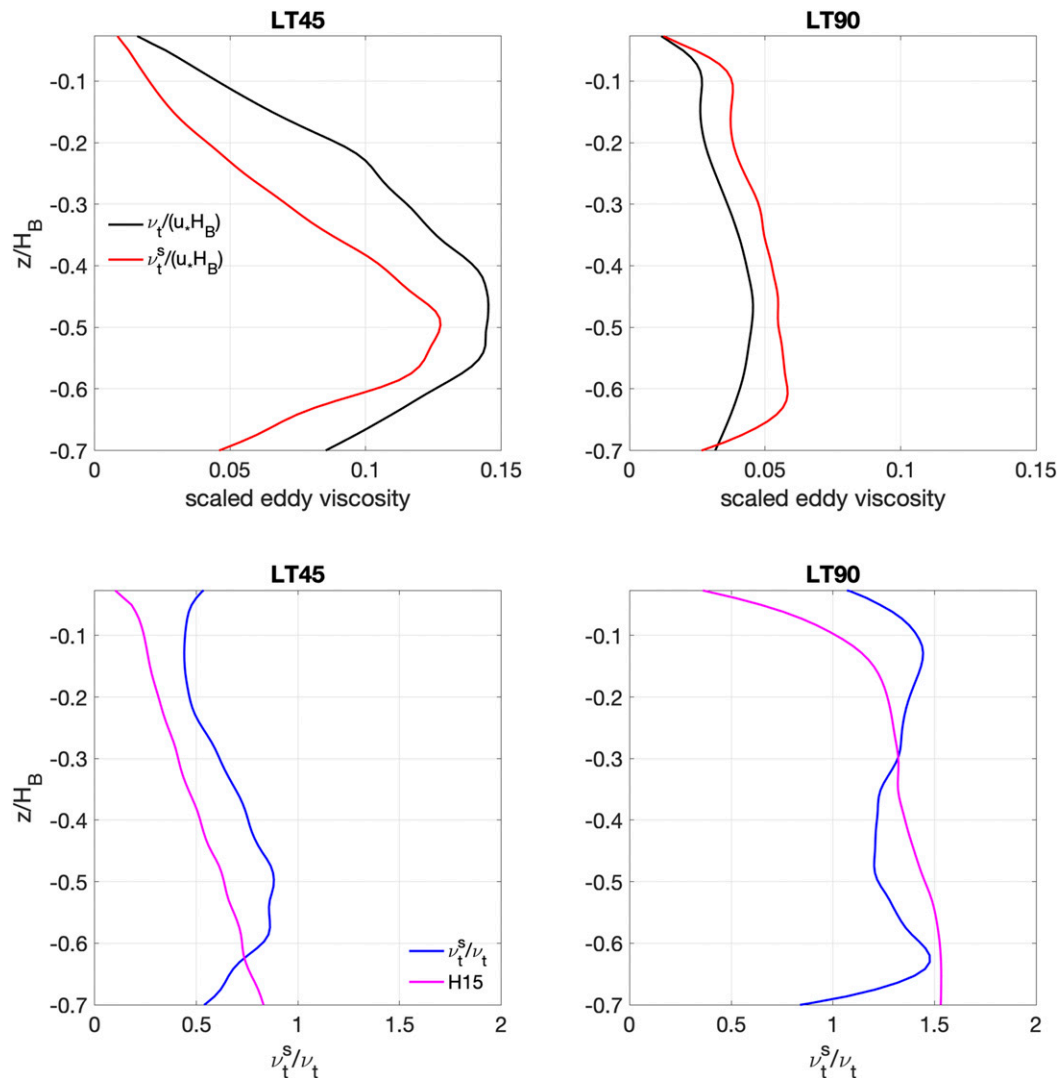


FIG. 6. (top) Scaled turbulent eddy viscosity for Eulerian shear ( $\nu_t$ , black solid line) and Stokes drift shear ( $\nu_t^s$ , red solid line) in (left) case LT45 and (right) LT90. (bottom) The ratios of  $\nu_t^s$  to  $\nu_t$  based on the LES results (blue solid line) and Harcourt (2015) model (H15) (magenta solid line). The eddy viscosity is scaled by  $u_* H_B$ , and all the variables are time averaged from  $t = 30$  h to  $t = 40$  h.

motivates further development for ARSMs under substantial wind-wave misalignments.

#### d. Generation of $\langle u'v' \rangle$ under wind-wave misalignments

The examination of stress budgets in the last section illustrates the important role of waves in stress production, which is through Stokes drift shear and velocity variances as well as the covariance of horizontal momentum  $\langle u'v' \rangle$ . Our comparison of Pstokes between case LT0 and LT45 suggests that  $\langle u'v' \rangle$  is not zero under large wind-wave misalignments and significantly influences Pstokes (section 3b). Thus, in this section we focus on assessing the evolution of  $\langle u'v' \rangle$  in cases LT45 and LT90, aiming to understand the mechanism of  $\langle u'v' \rangle$  generation and the role of  $\langle u'v' \rangle$  in controlling the Stokes drift shear stress production.

LT is characterized by counterrotating vortex pairs, which generate strong convergent regions that couple with significant downwelling jets near the surface (left and middle, Fig. 8). For case LT45, a large negative  $\langle u'v' \rangle$  is generated at  $z > -10$  m  $\langle u'v' \rangle$  and only decays slightly after 30 h, reaching a stationary state with a magnitude of twice  $\langle u'w' \rangle$  (left panel, Fig. 7). Substantial  $\langle u'v' \rangle$  coincides with the LT direction ( $\theta_{LT}$ ) that is not aligned or perpendicular to the wind direction ( $\theta_W$ ) (Fig. 8, center panel). Here,  $\theta_{LT}$  is objectively obtained from two-dimensional, horizontal two-point autocorrelation of the vertical velocities following Sullivan et al. (2012) and Wang et al. (2019). To conceptually illustrate the emergence of a nonnegligible  $\langle u'v' \rangle$ , we examine the horizontal structure of dominant Langmuir cells (short LCs) with conditional averages following (McWilliams et al. 1997; Kukulka et al. 2010; Wang et al. 2019). Considering that strong downwelling jets are

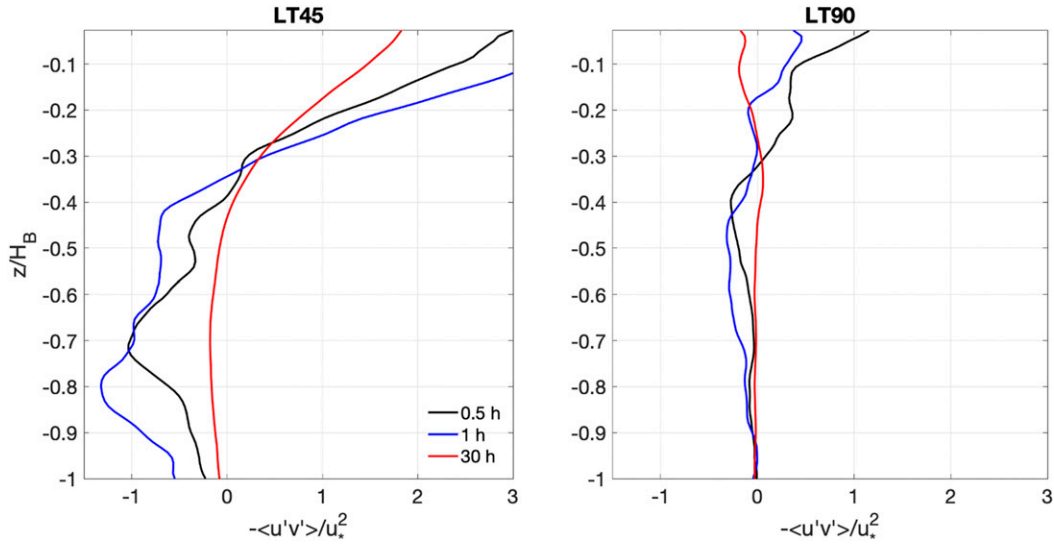


FIG. 7. The normalized  $-\langle u'v' \rangle$  by  $u_*^2$  at 0.5 h (black solid), 1 h (blue solid), and 30 h (red solid) for case (left) LT45 and (right) LT90.

common characteristics of LCs, we identify dominant LCs with a vertical velocity threshold  $w < -2\langle w^2 \rangle^{1/2}$  at the depth of maximum  $\langle w^2 \rangle$ , which are defined as LC events. This conditional average is denoted by  $\{ \dots \}$ .

For LT0, the map view of normalized  $\{w\}$  shows strong downwelling jets in the central region that couples with convergent horizontal anomalies ( $\{u'\}$ ,  $\{v'\}$ ) (left, Fig. 9). Since LC is aligned with the wind,  $\{u'\}$  is approximately zero, which results in a near-zero correlation of  $\{u'\}$  and  $\{v'\}$ . For LT45, however, the misalignment of these convergence regions with the wind direction introduces nonnegligible  $\{u'\}$  and  $\{v'\}$  that are negatively correlated leading to a finite  $\langle u'v' \rangle$  (right, Fig. 9). While flow structures are independent of the orientation of the coordinate system, specific values of  $\langle v'^2 \rangle$ , and  $\langle u'v' \rangle$  depend on the choice of coordinates. For instance, if we rotate the coordinate axes to make  $u$  along the LT direction,  $\langle u'v' \rangle$  will be zero in the new coordinate (assuming  $u$  is zero for idealized coherent LT roll vortices). However, the coordinate rotation will introduce extra

terms in the stress budgets for  $\langle u'w' \rangle$  and  $\langle v'w' \rangle$ , so that stress budgets in both coordinate systems are still equivalent. For case LT90, organized coherent Langmuir cell structures are much weaker because of a zero Stokes production (right, Fig. 8). As such, the absence of LT-induced convergent and divergent turbulent flows leads to the vanishing of  $\langle u'v' \rangle$  after 30 h (right panel, Fig. 7). Thus, LT-induced convergent and divergent flows that are not aligned with the  $x$  or  $y$  axes result in nonnegligible  $\langle u'v' \rangle$ .

To further understand the generation of  $\langle u'v' \rangle$  in case LT45, we investigate the Reynolds stress transport equation of  $\langle u'v' \rangle$  (Harcourt 2013):

$$\frac{\partial \langle u'v' \rangle}{\partial t} + \frac{\partial \langle u'v'w' \rangle}{\partial z} = - \left( \langle u'w' \rangle \frac{\partial \langle v' \rangle}{\partial z} + \langle v'w' \rangle \frac{\partial \langle u' \rangle}{\partial z} \right) - \frac{1}{\rho_0} \left( \left\langle \left\langle u' \frac{\partial p'}{\partial y} \right\rangle \right\rangle + \left\langle \left\langle v' \frac{\partial p'}{\partial x} \right\rangle \right\rangle \right) + \text{SGS}_{xy}, \tag{8}$$

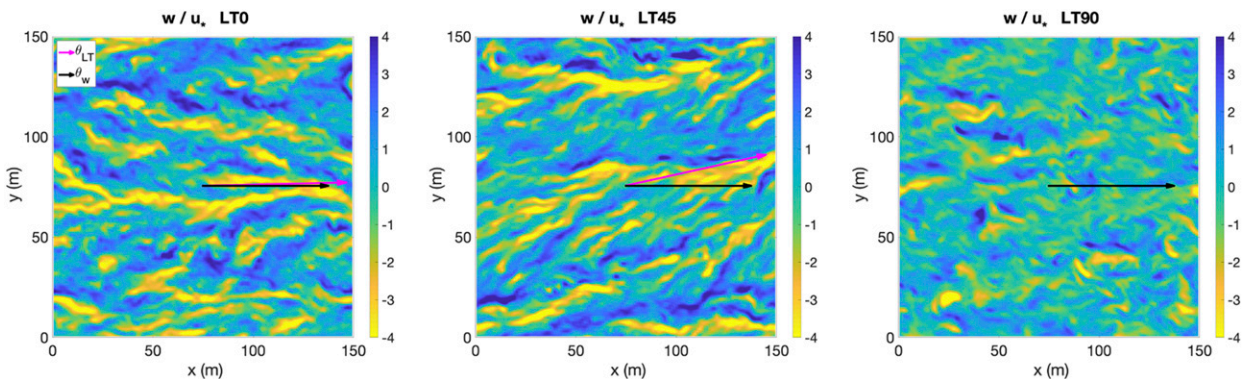


FIG. 8. The normalized vertical velocity field for cases (left) LT0, (center) LT45, and (right) LT90. The flow field is at the depth of the maximum vertical velocity variance. The black and magenta solid arrows indicate the wind direction and LT direction, respectively.

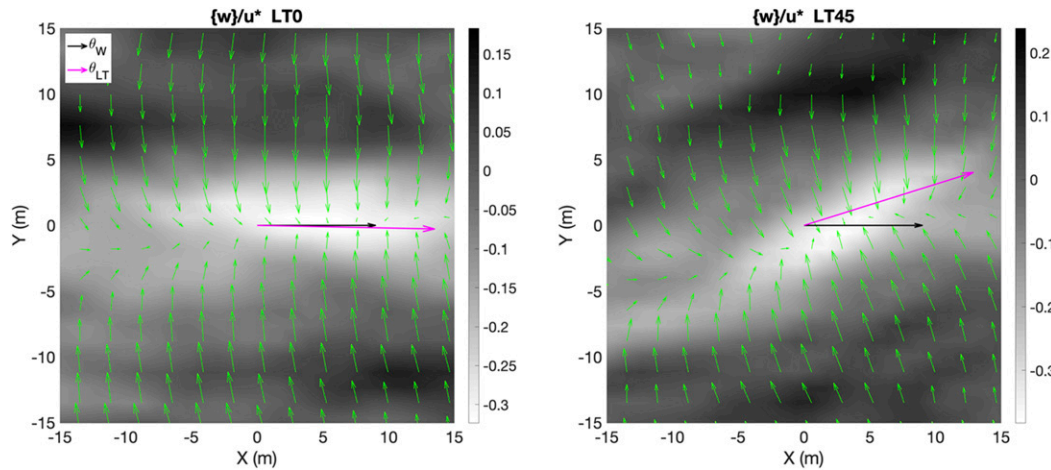


FIG. 9. Map view of normalized vertically averaged vertical velocity  $\{w\}$  at the depth of the maximum vertical velocity variance after the conditional average for (left) LT0 and (right) LT45. The magenta solid arrow shows the direction of LT, and the black solid arrow represents the wind direction. The green arrows indicate the anomalies of horizontally averaged velocity  $\{u'\}$ ,  $\{v'\}$  near the surface.

where the left-hand-side terms have the same physical meanings analogous to Eqs. (4) and (5) and the right-hand-side terms of Eq. (8) from left to right represent: the Eulerian shear stress production due to the misalignment between Reynolds stress (vertical momentum flux) and Eulerian shear (Pshear), VPG, and unresolved SGS terms ( $SGS_{xy}$ ). Note that there is no Stokes drift shear stress production in this direction. All budget terms are time-averaged between 30 and 40 h when the turbulence is steady (left, Fig. 10).

For case LT45 with wind-wave misalignments, the original alignment between Eulerian shear and Reynolds stress is distorted by the imposed crosswind Stokes drift, which induces a

negative stress production for  $\langle u'v' \rangle$  [refer to Eq. (8)] (black solid line, left panel, Fig. 10). Since the crosswind stress is approximately zero, this stress production (Pshear) is determined by the along-wind stress and the crosswind Eulerian shear and is approximately balanced by VPG (magenta solid line, left panel, Fig. 10). Given the presence of the crosswind Eulerian shear and along-wind Reynolds stress,  $\langle u'v' \rangle$  must be produced according to Eq. (8).

Since  $\langle u'v' \rangle$  is nonnegligible for LT45, we now assess its role in Stokes drift shear stress production that appears in the stress budgets for the vertical stress [refer to Eqs. (4) and (5)]. We find that the stress productions associated with  $\langle u'v' \rangle$  are

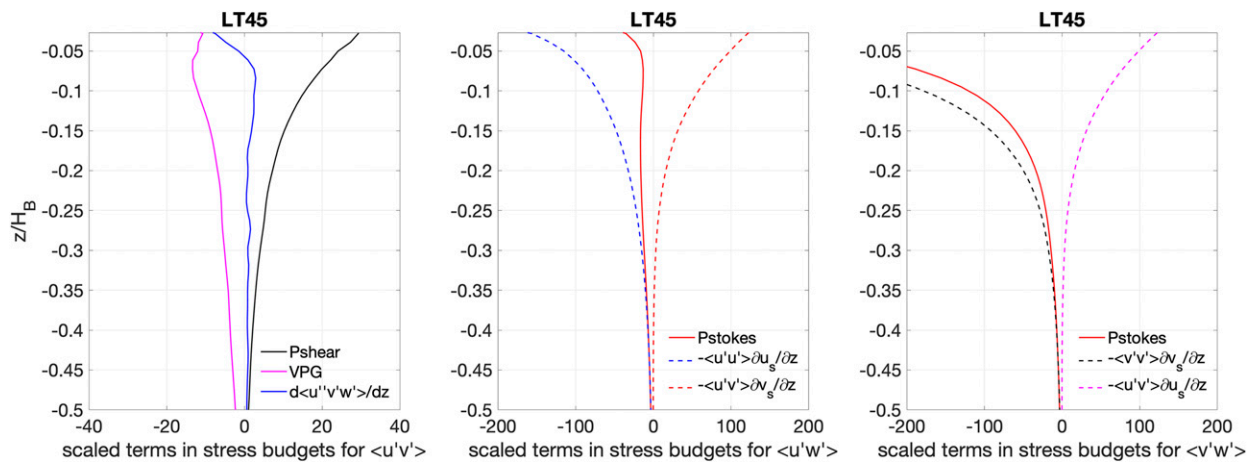


FIG. 10. Scaled terms in stress budget for (left) turbulent horizontal flux of horizontal momentum  $\langle u'v' \rangle$ , turbulent vertical flux of horizontal momentum for (center)  $\langle u'w' \rangle$  and (right)  $\langle v'w' \rangle$ . In the left panel, the Eulerian shear stress production (Pshear), VPG, and the vertical divergence of the horizontal turbulent momentum flux ( $d\langle u'v'w' \rangle/dz$ ) are denoted by black, magenta, and blue solid lines. Pstokes denotes the total Stokes drift shear stress production in the stress budgets for  $\langle u'w' \rangle$  in the center panel and  $\langle v'w' \rangle$  in the right panel and equals  $-\langle u'u' \rangle \partial u_s / \partial z - \langle u'v' \rangle \partial v_s / \partial z$  and  $-\langle v'v' \rangle \partial v_s / \partial z - \langle u'v' \rangle \partial u_s / \partial z$ , respectively. Note that these budgets are scaled by  $u_*^2/H_B$  and time averaged from  $t = 30$  h to  $t = 40$  h.

positive and are the same in both along-wind and crosswind directions because of the same  $u_s$  and  $v_s$  (left and center panels, red and magenta dashed lines, Fig. 10). The other part of the Stokes drift shear stress production is associated with the velocity variances, which is greater in the crosswind direction with the augmented crosswind velocity variances (Fig. 4). This also explains the much smaller along-wind  $P_{\text{Stokes}}$  in case LT45 than case LT0, which is due to the positive stress production by  $\langle u'v' \rangle$  (cases LT0 and LT45, top panels, Fig. 5). In summary,  $\langle u'v' \rangle$  is generally not zero and sea-state dependent in wind-wave misalignment conditions, which directly affects the budgets of vertical momentum fluxes that drive ocean currents.

#### 4. Conclusions

This study has investigated the relation between Reynolds stress and Lagrangian shear through idealized LES experiments with a constant wind and abruptly imposed Stokes drifts with different wind misalignment angles. To circumvent spiraling Ekman and inertial currents, the experiments exclude the Coriolis force and apply a body force that balances the wind stress.

We assess the profiles of mean currents and Reynolds stress in two stages: the early stage when the flow is transient and the adjustment is not complete, and the late stage when the flow is stationary. During the early transient stage, a crosswind Eulerian current that opposes the crosswind Stokes drift is generated in the cases with wind-wave misalignments. The examination of the stress profiles illustrates the generation of a crosswind Reynolds stress, which drives the crosswind Eulerian currents. However, this crosswind stress decays and vanishes in the late stage. Different from the diminished crosswind Reynolds stress, the crosswind Eulerian current is still present and reaches a stationary state in the late stage of the simulations. In addition, the Eulerian shear is neither zero nor does it cancel out the Stokes drift shear, yielding a nonzero Lagrangian shear in the crosswind direction. Consequently, the Lagrangian shear does not align with the Reynolds stress, which is along the wind direction.

To further investigate the relation between the stress and shear and also understand the evolution of stress in different directions, we examine the budgets for the Reynolds stress. For the case with aligned Stokes drift and wind, the predominant balance of stress budgets is between the Stokes drift shear stress production ( $P_{\text{Stokes}}$ ) and VPG. Only for the cases with wind-misaligned waves, are the crosswind stress budgets significant, with the presence of a negative  $P_{\text{Stokes}}$  and a positive Eulerian shear stress production ( $P_{\text{shear}}$ ). Thus, the different stress budgets reflect changes in the turbulence, which account for the emergence of the crosswind Eulerian current. As such, a nonzero crosswind Lagrangian shear is present, resulting in the misalignment between Reynolds stress and Lagrangian shear.

Our results are qualitatively consistent with an algebraic Reynolds stress model (ARSM) that is derived from the Craik–Leibovich equation (Harcourt 2013, 2015). However, substantial quantitative differences between LES and ARSM results near the surface are due to uncertainties of parameterizations in ARSMs,

particularly under substantial wind-wave misalignments (Harcourt 2015; Pearson et al. 2019). We also find that a turbulent horizontal flux of horizontal momentum ( $\langle u'v' \rangle$ ) is present in the case for which Stokes drift and wind are 45° misaligned (LT45), which is associated with wind-misaligned Langmuir cells. The examination of stress budget for  $\langle u'v' \rangle$  shows that it is the stress production by the along-wind stress and the crosswind Eulerian shear that generates  $\langle u'v' \rangle$ . This nonnegligible  $\langle u'v' \rangle$  plays an important role in controlling the Stokes drift shear stress production in the stress budget for  $\langle u'w' \rangle$  and  $\langle v'w' \rangle$ , which indirectly affects the vertical momentum flux that forces ocean current.

For existing turbulence parameterizations, however, the closure of ARSMs often utilizes the equilibrium solution of Eqs. (4) and (5) and is developed based on a limited set of LES experiments with small wind-wave misalignments (Kantha and Clayson 2004; Harcourt 2013, 2015; Pearson et al. 2019). As a result, neither the nonnegligible  $\langle u'v' \rangle$  for the strongly misaligned wind and waves nor the stress production by the Stokes drift shear and  $\langle u'v' \rangle$  [refer to Eqs. (4), (5)] has been accurately parameterized. In realistic ocean conditions, significant wind-wave misalignments are prevalent (Fan et al. 2009). Such misaligned wind wave conditions may be associated with a nonequilibrium wave field, which features complex sea states that are characterized by complex transient two-dimensional wave spectra with multiple energy peaks. Those complex sea states control the behavior of wave forcing, which directly influences the stress production by Stokes drift shear and thus are potentially important factors that need to be also considered in turbulence parameterizations. Thus, future work on improvements of turbulence parameterizations also requests sophisticated wind and wave modeling as well as observations to facilitate a more comprehensive understanding for the OSBL turbulence in conditions of strong wind and wave misalignment. To summarize, our study illustrates the complex relation between Reynolds stress, velocity shear and stress production through idealized LES experiments with different wind-wave misalignments, which is critical in understanding upper-ocean dynamics in realistic wind and wave forcing conditions.

*Acknowledgments.* We acknowledge the support of NSF Grants OCE-1634578 for funding this work. We wish to thank Pearson Brodie and Xingchi Wang for constructive and meaningful discussions. We also thank the high-performance computing resources as well as Information Technologies support from NCAR Large Computation Allocation Grant, sponsored by National Science Foundation, and University of Delaware's high-performance computers Mills and Farber. We thank two anonymous reviewers for their constructive comments, which have substantially improved the manuscript.

#### REFERENCES

- Craik, A. D. D., and S. Leibovich, 1976: A rational model for Langmuir circulations. *J. Fluid Mech.*, **73**, 401–426, <https://doi.org/10.1017/S0022112076001420>.
- D'Asaro, E. A., 2014: Turbulence in the upper-ocean mixed layer. *Annu. Rev. Mar. Sci.*, **6**, 101–115, <https://doi.org/10.1146/annurev-marine-010213-135138>.

- Deardorff, J. W., 1973: Use of subgrid transport equations in a three-dimensional model of atmospheric turbulence. *J. Fluids Eng.*, **95**, 429–438, <https://doi.org/10.1115/1.3447047>.
- Fan, Y., I. Ginis, T. Hara, C. W. Wright, and E. J. Walsh, 2009: Numerical simulations and observations of surface wave fields under an extreme tropical cyclone. *J. Phys. Oceanogr.*, **39**, 2097–2116, <https://doi.org/10.1175/2009JPO4224.1>.
- Farmer, D., and M. Li, 1995: Patterns of bubble clouds organized by Langmuir circulation. *J. Phys. Oceanogr.*, **25**, 1426–1440, [https://doi.org/10.1175/1520-0485\(1995\)025<C1426:POBCOB>E2.0.CO;2](https://doi.org/10.1175/1520-0485(1995)025<C1426:POBCOB>E2.0.CO;2).
- Gargett, A., J. Wells, A. E. Tejada-Martínez, and C. E. Grosch, 2004: Langmuir supercells: A mechanism for sediment resuspension and transport in shallow seas. *Science*, **306**, 1925–1928, <https://doi.org/10.1126/science.1100849>.
- Harcourt, R. R., 2013: A second-moment closure model of Langmuir turbulence in pure wind seas. *J. Phys. Oceanogr.*, **43**, 673–697, <https://doi.org/10.1175/JPO-D-12-0105.1>.
- , 2015: An improved second-moment closure model of Langmuir turbulence. *J. Phys. Oceanogr.*, **45**, 84–103, <https://doi.org/10.1175/JPO-D-14-0046.1>.
- , and E. A. D’Asaro, 2008: Large-eddy simulation of Langmuir turbulence in pure wind seas. *J. Phys. Oceanogr.*, **38**, 1542–1562, <https://doi.org/10.1175/2007JPO3842.1>.
- Kantha, L. H., and C. A. Clayson, 2004: On the effect of surface gravity waves on mixing in the oceanic mixed layer. *Ocean Modell.*, **6**, 101–124, [https://doi.org/10.1016/S1463-5003\(02\)00062-8](https://doi.org/10.1016/S1463-5003(02)00062-8).
- Kukulka, T., and F. Veron, 2019: Lagrangian investigation of wave-driven turbulence in the ocean surface boundary layer. *J. Phys. Oceanogr.*, **49**, 409–429, <https://doi.org/10.1175/JPO-D-18-0081.1>.
- , A. J. Plueddemann, J. H. Trowbridge, and P. P. Sullivan, 2009: Significance of Langmuir circulation in upper ocean mixing: Comparison of observations and simulations. *Geophys. Res. Lett.*, **36**, L10603, <https://doi.org/10.1029/2009GL037620>.
- , —, —, and —, 2010: Rapid mixed layer deepening by the combination of Langmuir and shear instabilities: A case study. *J. Phys. Oceanogr.*, **40**, 2381–2400, <https://doi.org/10.1175/2010JPO4403.1>.
- Large, W. G., E. G. Patton, and P. P. Sullivan, 2019: Nonlocal transport and implied viscosity and diffusivity throughout the boundary layer in LES of the Southern Ocean with surface waves. *J. Phys. Oceanogr.*, **49**, 2631–2652, <https://doi.org/10.1175/JPO-D-18-0202.1>.
- McWilliams, J. C., and P. P. Sullivan, 2000: Vertical mixing by Langmuir circulations. *Spill Sci. Technol. Bull.*, **6**, 225–237, [https://doi.org/10.1016/S1353-2561\(01\)00041-X](https://doi.org/10.1016/S1353-2561(01)00041-X).
- , —, and C.-H. Moeng, 1997: Langmuir turbulence in the ocean. *J. Fluid Mech.*, **334**, 1–30, <https://doi.org/10.1017/S0022112096004375>.
- , E. Huckle, J.-H. Liang, and P. P. Sullivan, 2012: The wavy Ekman layer: Langmuir circulations, breaking waves, and Reynolds stress. *J. Phys. Oceanogr.*, **42**, 1793–1816, <https://doi.org/10.1175/JPO-D-12-07.1>.
- Moeng, C.-H., 1984: A large-eddy-simulation model for the study of planetary boundary-layer turbulence. *J. Atmos. Sci.*, **41**, 2052–2062, [https://doi.org/10.1175/1520-0469\(1984\)041<2052:ALESMF>2.0.CO;2](https://doi.org/10.1175/1520-0469(1984)041<2052:ALESMF>2.0.CO;2).
- Pearson, B., 2018: Turbulence-induced anti-Stokes flow and the resulting limitations of large-eddy simulation. *J. Phys. Oceanogr.*, **48**, 117–122, <https://doi.org/10.1175/JPO-D-17-0208.1>.
- Pearson, B. C., A. L. M. Grant, and J. A. Polton, 2019: Pressure-strain terms in Langmuir turbulence. *J. Fluid Mech.*, **880**, 5–31, <https://doi.org/10.1017/jfm.2019.701>.
- Polton, J. A., D. M. Lewis, and S. E. Belcher, 2005: The role of wave-induced Coriolis–Stokes forcing on the wind-driven mixed layer. *J. Phys. Oceanogr.*, **35**, 444–457, <https://doi.org/10.1175/JPO2701.1>.
- , Y.-D. Lenn, S. Elipot, T. K. Chereskin, and J. Sprintall, 2013: Can Drake Passage observations match Ekman’s classic theory? *J. Phys. Oceanogr.*, **43**, 1733–1740, <https://doi.org/10.1175/JPO-D-13-034.1>.
- Rabe, T. J., T. Kukulka, I. Ginis, T. Hara, B. G. Reichl, E. A. D’Asaro, R. R. Harcourt, and P. P. Sullivan, 2015: Langmuir turbulence under Hurricane Gustav (2008). *J. Phys. Oceanogr.*, **45**, 657–677, <https://doi.org/10.1175/JPO-D-14-0030.1>.
- Reichl, B. G., D. Wang, T. Hara, I. Ginis, and T. Kukulka, 2016: Langmuir turbulence parameterization in tropical cyclone conditions. *J. Phys. Oceanogr.*, **46**, 863–886, <https://doi.org/10.1175/JPO-D-15-0106.1>.
- Sullivan, P. P., J. C. McWilliams, and C. Moeng, 1994: A subgrid-scale model for large-eddy simulation of planetary boundary-layer flows. *Bound.-Layer Meteor.*, **71**, 247–276, <https://doi.org/10.1007/BF00713741>.
- , L. Romero, J. C. McWilliams, and W. K. Melville, 2012: Transient evolution of Langmuir turbulence in ocean boundary layers driven by hurricane winds and waves. *J. Phys. Oceanogr.*, **42**, 1959–1980, <https://doi.org/10.1175/JPO-D-12-025.1>.
- Teixeira, M. A., 2018: A model for the wind-driven current in the wavy oceanic surface layer: Apparent friction velocity reduction and roughness length enhancement. *J. Phys. Oceanogr.*, **48**, 2721–2736, <https://doi.org/10.1175/JPO-D-18-0086.1>.
- Thorpe, S., 2004: Langmuir circulation. *Annu. Rev. Fluid Mech.*, **36**, 55–79, <https://doi.org/10.1146/annurev.fluid.36.052203.071431>.
- Wang, D., T. Kukulka, B. G. Reichl, T. Hara, I. Ginis, and P. P. Sullivan, 2018: Interaction of Langmuir turbulence and inertial currents in the ocean surface boundary layer under tropical cyclones. *J. Phys. Oceanogr.*, **48**, 1921–1940, <https://doi.org/10.1175/JPO-D-17-0258.1>.
- , —, —, —, and —, 2019: Wind-wave misalignment effects on Langmuir turbulence in tropical cyclones conditions. *J. Phys. Oceanogr.*, **49**, 3109–3126, <https://doi.org/10.1175/JPO-D-19-0093.1>.
- Weller, R. A., and J. F. Price, 1988: Langmuir circulations within the oceanic mixed layer. *Deep-Sea Res.*, **35**, 711–747, [https://doi.org/10.1016/0198-0149\(88\)90027-1](https://doi.org/10.1016/0198-0149(88)90027-1).